ADVANCED FUNCTIONAL MATERIALS
www.afm-journal.de

Oxygen Vacancy-Rich Defects Porous $Cu_2MgO_3/Mg_{0.78}Cu_{0.22}O$ Composite with Sinter-Resistant and Highly Reactive for Long-Duration High-Temperature Thermochemical Energy Storage

*Jiali Deng, Changdong Gu, Haoran Xu, Peiwang Zhu, and Gang Xiao**

High-temperature thermochemical energy storage based on metal oxides is the key technology to reducing the levelized costs of electricity of the next-generation concentrated solar power plants. CuO/Cu_2O has wide availability and high energy density, but severe sintering leads to low reactivity. In this study, an innovative approach to modulate the oxygen vacancy content to change the surface properties and crystal structure to enhance the sintering resistance and redox reversibility is proposed. The re-oxidation degree is increased from 46% to 99%, and the energy release rate is increased by 3.5 times. It remains 99.9% reduction and 97.1% oxidation activity after 3000 cycles, which is very valuable for engineering applications. Cu_2MgO_3 and $Mg_{0.78}Cu_{0.22}O$ are prone to form oxygen vacancies, which promotes the formation of porous structures. $Mg0_{.78}Cu_{0.22}O$ helps $Cu_2MgO_3/CuO/Cu_2O$ deliver more O through the surface. $Mg_{0.78}Cu_{0.22}O$ is firmly and uniformly dispersed on the CuO/Cu_2O surface after long cycling. They have a large binding energy, more charge transfer and enhanced bond energy at the interface. The mechanism of composite in increasing the sintering temperature and long-term reaction stability is revealed from experimental and theoretical calculations, which provides a new idea for the rational design of thermochemical energy storage materials.

1. Introduction

Concentrated solar power (CSP) system is considered as one of the most promising large-scale renewable electricity sources, especially when equipped with thermal energy storage technology that can effectively address the challenges of solar intermittent and deliver cost-effective base-load and dispatchable power.[1] In the third-generation CSP plants, the need for higher temperature storage media to increase the thermodynamic cycle efficiency is regarded as the key way to reduce the levelized costs of electricity.[2] Compared to other storage technologies, thermochemical energy storage is an attractive scheme due to its higher operating temperature, energy density, long-term storage, negligible heat loss, and easier transportation.[3] Among them, the metal oxide system has fast reaction kinetics. Air is both the reaction medium and the heat transfer fluid. There is no need for a high-pressure gas storage device, which significantly reduces the complexity of the system.[4] Co_3O_4/CoO, Mn_2O_3/Mn_3O_4 and CuO/Cu_2O are favored candidates and have been extensively studied by researchers.[5–7] Co_3O_4/CoO has high reaction enthalpy and good redox characteristics, but the material is toxic and costly.[8–12] Mn_2O_3/Mn_3O_4 has very slow oxidation and low cyclic stability, but the performance can be greatly improved by doping Fe, Si, Al, Cr, and Mo, etc.[13–17] However, its energy density is still much smaller than that of other redox couples and a large hysteresis interval between oxidation and reduction leads to adverse effects on the exergetic efficiency of the process.[18] CuO/Cu_2O system has the advantages of high energy density, abundant resources, non-toxicity and relatively low cost.[4–7] However, the reduction temperature is about 1020 °C and close to the melting point temperature of Cu_2O at 1235 °C.[19] The high temperature leads to serious sintering problems, resulting in low reactivity and short cycle life.[20] It greatly limits its application prospects.

Alonso[21] studied the reactivity of CuO in air or Ar atmosphere. The results showed that it was stronger coalescence of the particles in air with a reduction conversion rate of only 40% but 80% in Ar. And the temperature of oxygen release in air was 800 °C higher than that in argon (500 °C) by 300 °C. Deutsch[22] adjusted the atmosphere of the reduction reaction to N_2 for experimental exploration. It was found that the reduction

J. Deng, H. Xu, P. Zhu, G. Xiao
Key Laboratory of Clean Energy and Carbon Neutrality of Zhejiang Province, State Key Laboratory of Clean Energy Utilization, College of Energy Engineering
Zhejiang University
Hangzhou, Zhejiang 310027, China
E-mail: xiaogangtianmen@zju.edu.cn
C. Gu
State Key Laboratory of Silicon Materials, College of Materials Science and Engineering
Zhejiang University
Hangzhou, Zhejiang 310027, China

The ORCID identification number(s) for the author(s) of this article can be found under https://doi.org/10.1002/adfm.202315529

DOI: 10.1002/adfm.202315529

temperature of CuO could be reduced to 950 °C and that it exhibited excellent cycling stability over 20 cycles. Although the reaction temperature can be lowered by adjusting the atmosphere. But it is necessary to add corresponding high-precision control and gas storage devices, which will significantly increase the complexity and cost of the system. Gigantino[23] investigated a synthesis method for the preparation of porous CuO-based particles using yttria-stabilized zirconia (YSZ) as the sintering inhibitor. The 50 wt% CuO-YSZ particles exhibited good sintering resistance and a high reversible redox conversion rate after 100 consecutive cycles. However, YSZ is expensive and needs to add 50 wt% to achieve better effect, which is not suitable for large-scale application. In previous work, we reported the introduction of lower cost and higher thermally stable Al_2O_3, $MgCr_2O_4$ and $NiAl_2O_4$ to modify the surface of CuO/Cu_2O, which greatly improved the sintering temperature and re-oxidation performance.[24–26] In general, the current methods of mitigating sintering are basically by adjusting the reaction atmosphere to reduce the reaction temperature or artificially adding inert additives to form steric hindrance. It is worth noting that sintering causes particle densification. The reactive sites on the surface are greatly reduced and oxygen ions cannot diffuse inward, resulting in poor re-oxidation. For thermochemical energy storage materials, the improvement of sintering resistance and the increase of oxygen vacancy defects to promote O^{2-} diffusion need to be considered in both the reduction and oxidation processes. Therefore, we proposed a new research idea to regulate the oxygen vacancy content through appropriate doping. The surface properties of the metal oxides were modified to promote porous structure formation. It also changed the crystal structure and introduced vacancies to accelerate oxygen diffusion. The anti-sintering performance and redox reactivity were improved. Numerous studies in the field of catalysis have proved that Mg doping can help to create more defects in the material.[27,28] The radius of Mg has a large difference with that of Cu, which is easy to create defects in the crystal structure. Therefore, we chose Mg element for doping of Cu-based thermochemical energy storage material. In addition, the practical engineering application should pay full attention to the cycle life of thermochemical energy storage materials. However, the reported modified copper-based materials are basically less than 100 cycles. We verified the positive effects of the proposed method for 3000 cycles.

In this study, we constructed an oxygen vacancy-rich porous $Cu_2MgO_3/Mg_{0.78}Cu_{0.22}O$ composite structure. The spontaneously generated $Mg_{0.78}Cu_{0.22}O$ can help Cu_2MgO_3 to form a porous structure to resist sintering. And it also can deliver O through the surface to accelerate the reaction. First, we verified by DFT calculations that the oxygen vacancy formation energy on the surface of Cu_2MgO_3 was lower than that of CuO, which was easy to construct oxygen vacancy defects. Therefore, the composite was further prepared by a simple high-temperature heat treatment method. The composite was labeled Cu-Mg-O. It had successfully achieved the great improvement of long-term high-temperature anti-sintering and reactivity. The crystal structure, microstructure and chemical composition of the composite were characterized. Combined with theoretical computational analysis, the redox reaction mechanism and interaction relationship were described. The mechanism of improving sintering resistance and long-term cycling performance of the composite was also revealed. The effectiveness of this method was confirmed. It provides a new insight to alleviate the sintering problem of metal oxides and a new idea for the rational design of long-life and high-activity thermochemical energy storage materials.

2. Results and Discussion

2.1. Calculation of Oxygen Vacancy Formation Energy and Characterization of As-Prepared Sample

The formation energy of oxygen vacancies $E(V_O)$ on the surface of the material was calculated by DFT. Figure S2 (Supporting Information) shows the calculation results of $E(V_O)$ at different positions on the surface of Cu_2MgO_3 (100). The more stable structure of Cu_2MgO_3 (100) was determined. The calculation results in **Figure 1a** clearly show that the $E(V_O)$ on the Cu_2MgO_3 (100) surface (1.345 eV) is smaller than that of CuO (111) (1.433 eV). It indicated that the surface of Cu_2MgO_3 was easier to construct oxygen vacancy defects. Therefore, Cu_2MgO_3 was prepared to verify the effectiveness of the method that could achieve high-temperature sintering resistance and improve reactivity of materials with oxygen-rich vacancy defects. The physicochemical properties of the as-prepared samples were characterized, as shown in Figure 1 and Figure S3 (Supporting Information). The phase composition of Cu-Mg-O was analyzed by XRD. As shown in Figure 1b, all strong diffraction peaks can be indexed as Cu_2MgO_3 (ICDD-PDF No.41-1365) without other impurities. Figure 1c depicts the FTIR spectrum. The absorption bands of 432, 500, 596, 1402, 1639 cm^{-1} was ascribed to Cu^{2+}-O^{2-} and Mg^{2+}-O^{2-}.[29,30] The chemical state of the fresh sample was identified by XPS. The XPS spectra of Cu 2p are demonstrated in Figure 1d, where contains Cu 2p1/2 and Cu 2p3/2 along with the satellites, respectively. The peak with binding energy at 933.6 and 953.3 eV and the shake-up satellites corresponded to Cu^{2+}.[31] The Mg 1s spectra is shown in Figure 1e, where the peak at 1303.6 eV belongs to Mg^{2+}.[32] Figure 1f compares the O1s spectra of the prepared sample and pure CuO. Two typical peaks at 529.2-530.3 and 530.7-531.6 eV were attributed to lattice oxygen and adsorbed oxygen.[33] The peak attributed to adsorbed oxygen included the surface oxygen vacancies of the material and some oxygen substances adsorbed on the surface (such as OH^- or CO^{3-}, etc.). The adsorbed oxygen content of Cu-Mg-O was 80.90%, which was much higher than that of CuO (60.21%). Low-temperature EPR was further employed to jointly identify the oxygen vacancy concentration. As shown in Figure S3c (Supporting Information), an obvious signal attributed to oxygen vacancies appears at g = 2.003. The results showed that the signal of Cu-Mg-O at g = 2.003 was significantly higher than that of undoped CuO, suggesting that the as-prepared Cu-Mg-O had higher oxygen vacancy concentration. The low-temperature EPR test results are consistent with the XPS analysis in Figure 1f. It showed that the prepared composite had more oxygen defects. As shown in Figure 1g, pure CuO particles readily aggregate to form tightly bound large aggregates. However, Cu-Mg-O presented a porous structure, which was more conducive to mass and heat transfer. The corresponding EDS mapping of Cu-Mg-O showed that Cu, Mg and

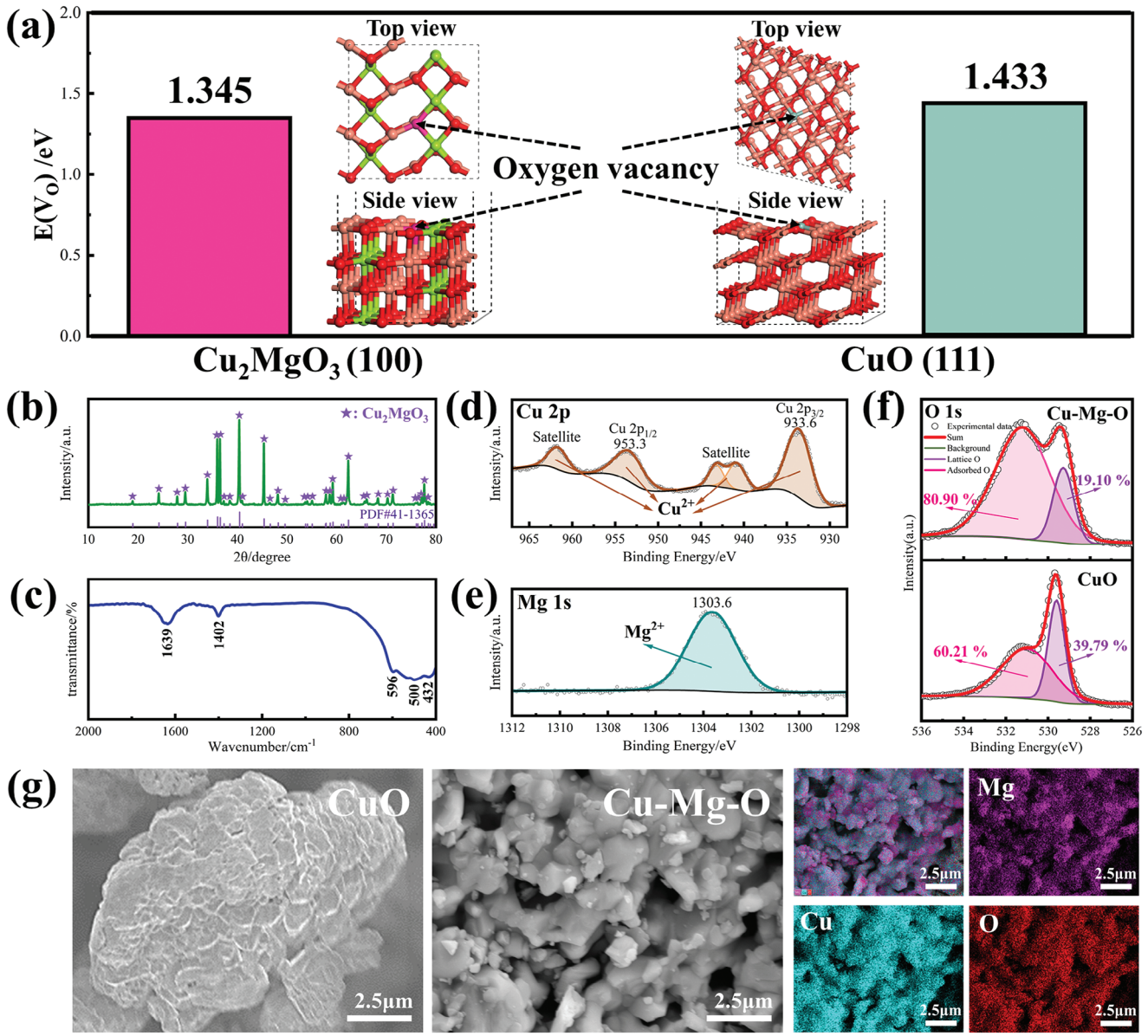

Figure 1. a) Formation energy of oxygen vacancies E(V_O) on the surface of Cu_2MgO_3 (100) and CuO (111). Physicochemical characterizations of fresh sample. b) XRD pattern. c) FTIR spectra. XPS spectra of d) Cu 2p, e) Mg 1s and f) O1s. g) FESEM images and corresponding EDS elemental mappings.

O element were uniformly distributed. These results proved the successful synthesis of porous Cu_2MgO_3 rich in oxygen vacancy defects.

2.2. Sinter Resistance at High Temperatures

The sintering resistance of Cu-Mg-O at high temperature was explored. The degree of sintering of the sample in the operating temperature range is shown in **Figure 2** and Figure S4 (Supporting Information). It could be observed that Cu-Mg-O maintained the porous structure, which only showed slight agglomeration between particles at the maximum operating temperature (1100 °C). The porous structure helped to distribute heat and gas evenly, which could effectively improve sinter resistance. Thus, the specific surface area of the material was increased to promote the diffusion and reaction of oxygen on the surface for improving the reactivity. However, CuO particles had begun to sinter severely at 1000 °C to form dense large agglomerates (≈15 μm), melt at 1040 °C and further densify into hard lumps (≈23 μm), and melt completely at 1060 °C (≈26 μm). It was worth mentioning that the CuO sample only showed severe sintering but did not melt before the reduction reaction temperature (≈1020 °C). It could undergo the reduction to convert into Cu_2O. But Cu_2O had poor high-temperature stability and low melting point. Therefore, it was speculated that the melting phenomenon was caused by Cu_2O, and the severe sintering of CuO before the reduction promoted the melting process.[25,26] Therefore, the

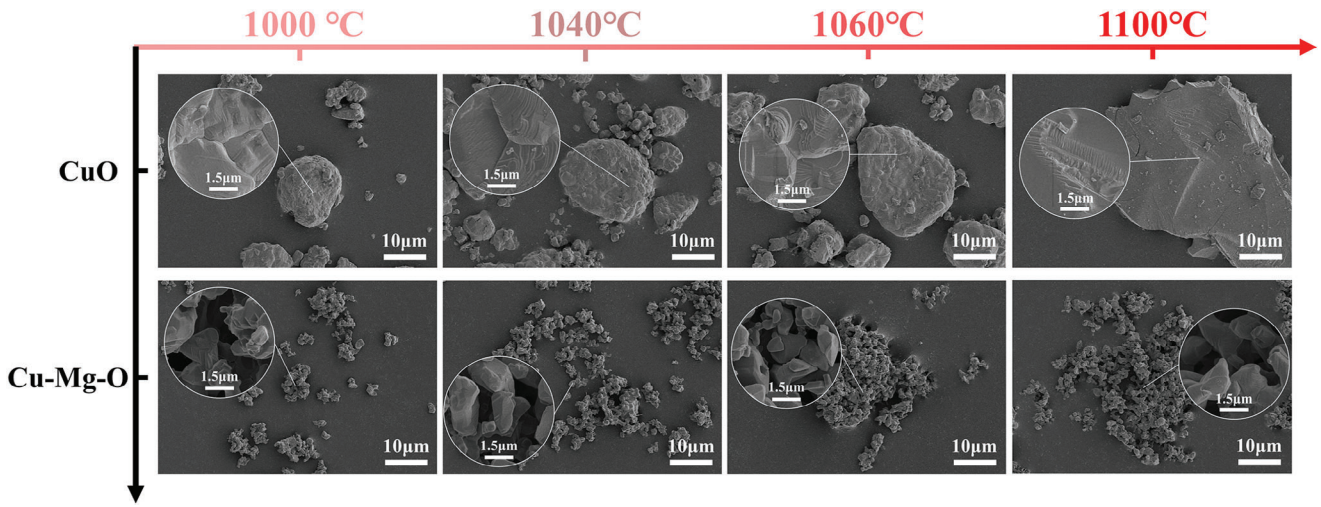

Figure 2. The degree of sintering in the working temperature range.

reactive sites on the surface were greatly reduced, which affected its re-oxidation performance.

2.3. Thermochemical Energy Storage Performance

The thermochemical reaction characteristics of the first cycle of Cu-Mg-O were tested by TGA/DSC3+ (**Figure 3**). Figure 3a displays the endothermic enthalpy change of CuO up to −993.577 Kj kg^{-1} during reduction, but the exothermic only 291.753 kJ kg^{-1} during oxidation. As shown in Figure 3b,c, the energy storage density of Cu-Mg-O is −362.822 kJ kg^{-1}, because its reduction weight loss ratio is 7.07% lower than that of CuO (10.02%). But its energy release density was as high as 357.009 kJ kg^{-1}. Because it was worth mentioning that compared with the re-oxidation degree of CuO was 46%, Cu-Mg-O reached more than 99%. These indicated that Cu-Mg-O had excellent chemical reversibility. Therefore, consistent with the analysis of Figure 2, improving the sintering resistance of copper-based materials can effectively promote redox reactions. In addition, Cu-Mg-O demonstrated faster redox reaction kinetics, especially in the energy release stage. The reduction reaction time was reduced from 13.22 to 3.81 min, and the reaction rate was increased by 3.5 times (Figure 3d).

2.4. Evolution of Microstructure and Morphology During Redox

In order to explore the changes of Cu-Mg-O with rich oxygen vacancies during redox to reveal the reasons for its excellent

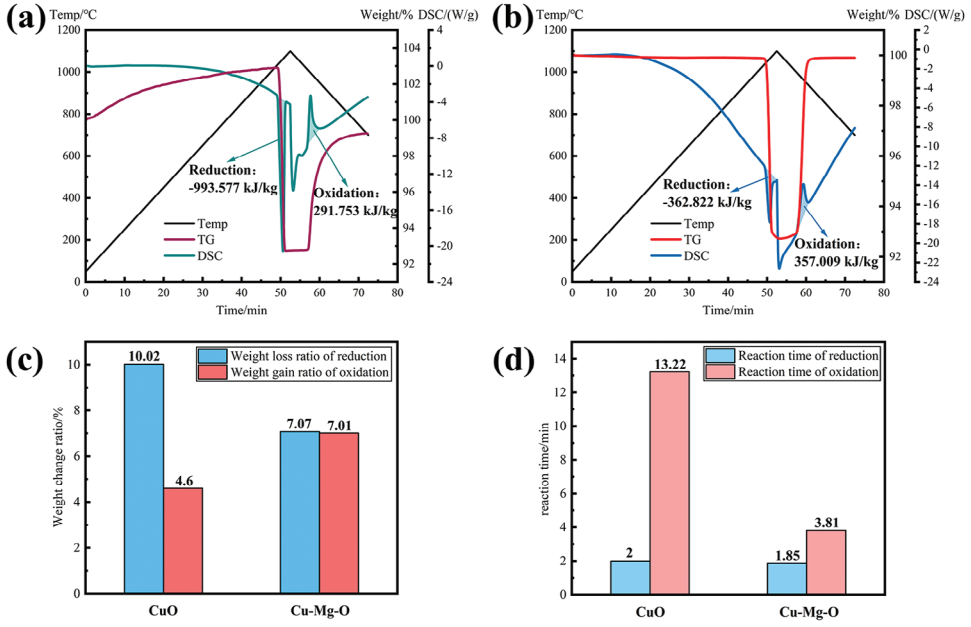

Figure 3. Comparison of thermochemical reaction performance. DSC curves of a) CuO and b) Cu-Mg-O. c) Weight change ratio. d) Reaction time.

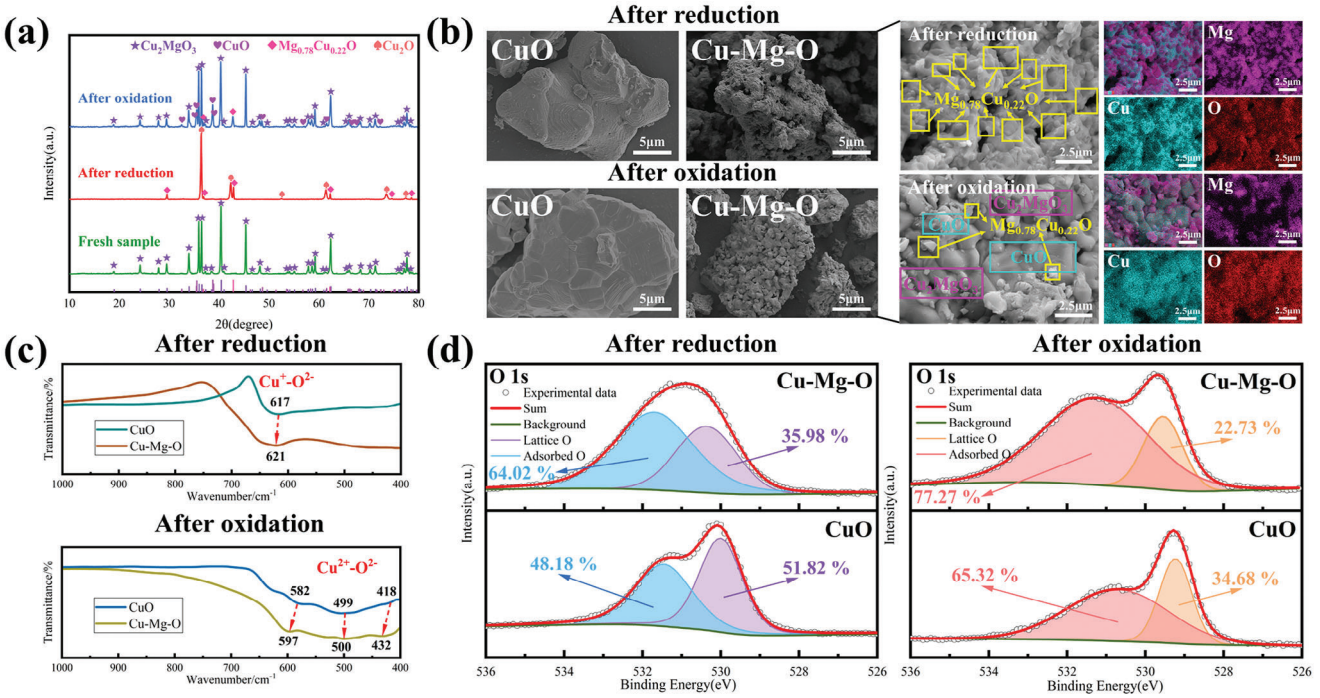

Figure 4. Characterization of microstructure and morphology during redox. a) XRD pattern. b) FESEM images and higher-magnification EDS elemental mappings. c) Local enlargement FTIR spectra at the range of 1000–400 cm^{-1}. d) XPS spectra of O 1s.

performance, we analyze the evolution of its microstructure and morphology, as shown in **Figure 4**. The crystal structure transformation of samples during the redox was characterized by XRD. The XRD pattern of pure CuO is shown in Figure S5 (Supporting Information), and there is still a large amount of Cu_2O in the oxidized sample. The results show that Cu_2O is not completely oxidized to CuO, and the re-oxidation performance is poor, which is consistent with the results in Figure 3. Figure 4a and Figure S6 (Supporting Information) demonstrate the reaction process of Cu-Mg-O. The reduction process is described in Equation 1, where Cu_2MgO_3 is converted to Cu_2O and $Mg_{0.78}Cu_{0.22}O$ while releasing oxygen and storing energy. The oxidized sample was composed of Cu_2MgO_3, CuO and $Mg_{0.78}Cu_{0.22}O$. After the oxidation reaction, the diffraction peak intensity of Cu_2MgO_3 was the strongest. It showed that the oxidized sample contained the highest content of Cu_2MgO_3. That was, most of the Cu_2O + $Mg_{0.78}Cu_{0.22}O$ underwent a reversible oxidation reaction to generate Cu_2MgO_3. In addition, there were diffraction peaks of CuO in the oxidized sample. It indicated that a small amount of Cu_2O is directly oxidized to CuO. As a result, the remaining small amount of $Mg_{0.78}Cu_{0.22}O$ couldn't be oxidized with enough Cu_2O to form Cu_2MgO_3. Thus, $Mg_{0.78}Cu_{0.22}O$ was retained after the oxidation. In other words, there are two reactions of $Cu_2O + Mg_{0.78}Cu_{0.22}O + O_2$ to form Cu_2MgO_3 (Equation 1) and the oxidation of a small amount of Cu_2O to CuO (Equation 2) occurred simultaneously during the re-oxidation. Therefore, the redox reaction in the subsequent cycle can be described by Equation 3.

$$Cu_2MgO_3 \rightleftharpoons 0.859Cu_2O + 1.282Mg_{0.78}Cu_{0.22}O + 0.4295O_2 \quad (1)$$

$$2Cu_2O + O_2 \rightleftharpoons 4CuO \quad (2)$$

$$2.859Cu_2O + 2.282Mg_{0.78}Cu_{0.22}O + 1.4295O_2 \rightleftharpoons 4CuO + Cu_2MgO_3 + Mg_{0.78}Cu_{0.22}O \quad (3)$$

Figure 4b shows the FESEM images of pure CuO and Cu-Mg-O at different reaction stages. After the reduction of CuO, the particles were severely sintered to form large particles with irregular shape. This led to a sharp decrease in the chemical reaction contact area between the material and air. Moreover, oxygen could only react with the surface of Cu_2O particles, but was difficult to diffuse into the interior, making the degree of re-oxidation low. This explains the results in Figure 3. As shown in Figure 3a,b, the thermochemical energy storage material undergoes a reduction reaction (energy storage) before oxidation (energy release). Therefore, the material needed to reach the initial temperature (≈1020 °C) of reduction reaction first to complete the reduction process and then reach the initial temperature (≈ 990 °C) of oxidation reaction for the oxidation. That was, the material needed to undergo a high temperature of up to 1100 °C before the oxidation process occurred to allow the reduction process to complete. Overall, the oxidized sample underwent a higher temperature (1100 °C) and stayed at the higher temperature for a longer period of time. Therefore, the material experienced a harsher environment after the oxidation than after the reduction. The oxidized particles aggregated further than the reduced sample. Thus, further sintering after oxidation of pure CuO aggravated the growth and densification of the particles. However, it could be clearly observed that Cu-Mg-O exhibited the porous structure during all reaction stages. This facilitated more oxygen to react on the surface of the material and diffuse internally, promoting the redox reaction. Therefore, although Cu-Mg-O showed

further aggregation after oxidation than after reduction, it had little effect on its reaction performance. Compared with pure CuO, it still exhibited excellent chemical reaction reversibility. The microstructure and phase distribution of Cu-Mg-O during the thermochemical reaction were further explored by higher-magnification EDS mapping. It could be clearly observed that $Mg_{0.78}Cu_{0.22}O$ was uniformly embedded on the surface of Cu_2O in the reduced sample. $Mg_{0.78}Cu_{0.22}O$ could prevent the sintering and densification of Cu_2O caused by the contact between grains. In addition, Cu_2MgO_3, CuO and $Mg_{0.78}Cu_{0.22}O$ were observed to be distributed in the oxidized samples (Figure 4b and Figure S7, Supporting Information). Corresponding to Figure 4a, most of Cu_2O and $Mg_{0.78}Cu_{0.22}O$ are oxidized to Cu_2MgO_3 during the oxidation. The remaining small amount of Cu_2O was oxidized to CuO, and $Mg_{0.78}Cu_{0.22}O$ was retained to alleviate the sintering of CuO. It was worth mentioning that the presence of $Mg_{0.78}Cu_{0.22}O$ in the redox process hindered the contact sintering between Cu_2O/CuO, which was conducive to the formation of porous structure.

The local enlargement FTIR spectra at the range of 1000–400 cm^{-1} is shown in Figure 4c. The absorption peak appeared at 617–621 cm^{-1} in the reduced sample, corresponding to the vibration of Cu^{+}-O^{2-}.[34] It could be found that the peak of Cu-Mg-O after reduction was shifted to a higher wavenumber. It suggested that there was a strong interaction between Cu_2O and $Mg_{0.78}Cu_{0.22}O$. Therefore, $Mg_{0.78}Cu_{0.22}O$ could be firmly embedded in the Cu_2O surface and was not easy to fall off during the high-temperature redox reaction. This effectively hindered the movement of Cu_2O grain boundaries and inhibited the growth of grains. Bands at 418–432, 499–500, and 582–597 cm^{-1} could be attributed to the vibration of Cu^{2+}-O^{2-}.[35] It was worth mentioning that the peak of Cu-Mg-O after oxidation also found the phenomenon of movement, indicating that there were also interactions between Cu_2MgO_3, CuO and $Mg_{0.78}Cu_{0.22}O$. $Mg_{0.78}Cu_{0.22}O$ also effectively inhibited CuO sintering during the oxidation.

Figure 4d shows the results of O1s XPS spectra of different samples during the redox. It could be clearly observed that the adsorbed oxygen content of the reduced Cu-Mg-O sample was 64.02%, which was higher than that of CuO (48.18%). The low-temperature EPR results of Figure S8a (Supporting Information) also clearly show that the reduced Cu-Mg-O has a stronger oxygen vacancy signal than CuO. It showed that the oxygen vacancies increased after the appearance of $Mg_{0.78}Cu_{0.22}O$ in the reduction product. $Mg_{0.78}Cu_{0.22}O$ provided a part of oxygen vacancies. It indicated that the surface of $Mg_{0.78}Cu_{0.22}O$ was easy to form oxygen vacancies, which could be transferred to Cu_2O after adsorbing oxygen. It helped Cu_2O capture more oxygen for easier and faster reaction, thereby greatly improving the re-oxidation performance and reaction rate (Figure 3). In addition, the sample after oxidation of Cu-Mg-O still had more adsorbed oxygen content than pure CuO. And as shown in Figure S8b (Supporting Information), the oxygen vacancy concentration of Cu-Mg-O after oxidation is higher than that of CuO. It was speculated that part of the contribution came from a small amount of $Mg_{0.78}Cu_{0.22}O$ in the sample. More because Cu_2MgO_3 itself had more oxygen vacancies, which could facilitate the internal diffusion and surface desorption of oxygen. This effectively improved the reduction reaction kinetics (Figure 3d). Therefore, $Mg_{0.78}Cu_{0.22}O$ could resist sintering while also helped Cu_2MgO_3/CuO/Cu_2O transfer O through surface oxygen vacancies for further enhancing redox reactivity. In addition, a large number of surface oxygen vacancy defects during the redox tended to aggregate and merge, thereby promoting the formation of porous structures.

2.5. Cycling Stability

The cycle stability of thermochemical energy storage materials directly affects the cost of the system, so it is a very important parameter in practical applications. We test the cycle performance of Cu-Mg-O for up to 3000 cycles, and the results are shown in **Figure 5** and Figure S9 (Supporting Information). As shown in Figure 5a,b, it maintains a reduction conversion rate of 99.9% during 3000 cycles. And the oxidation degree still remained 97.1% after 3000 cycles. But the undoped CuO had only 28% oxidation activity after 40 cycles (Figure S10, Supporting Information). It was worth noting that the oxidation activity of Cu-Mg-O decreased from 99% in the first cycle to 97.6% in the 600th cycle, and the conversion rate was basically stable at about 97% in the subsequent cycle. Figure 5c,d shows FESEM images of different reaction stages after cycles. It could be found that the grain size increased rapidly from 1 to 600 cycles, which was due to the difference in surface energy of different grain sizes, driving the aggregation and merging of grains at high temperature (Ostwald ripening).[13] As a result, the oxidation performance had a certain degree of attenuation. After 600 cycles, the particle size of Cu-Mg-O changed less, so the reaction performance began to remain stable. But it was worth noting that although the particle size change was relatively less after 600 cycles, the particles continued to aggregate slowly with the increase of the number of cycles. It should be noted that the thermochemical energy storage materials needed to be repeatedly cycled at a high temperature of 1100 °C. In particular, up to 3000 cycles were tested in this study. Therefore, the aggregation of Cu-Mg-O particles will still inevitably occur under the effect of high temperature for a long time. However, pure CuO showed serious agglomeration and sintering after only 10 cycles. And the grain boundaries of the sintered body were blurred and obviously densified after 40 cycles (Figure S11, Supporting Information). Surprisingly, although Cu-Mg-O also aggregated after 3000 cycles, there was no obvious sintering and densification, which was still much better than that of pure CuO after 40 cycles. Moreover, Cu-Mg-O maintained the porous structure well during 3000 cycles, indicating that it could effectively resist sintering and promote the reaction during high temperature and long cycle. Although the particles of Cu-Mg-O aggregated to a certain extent after long cycles, it had little effect on the reaction performance. Therefore, it could maintain 97.1% reactivity after 3000 cycles. In addition, EDS mapping of Cu-Mg-O after 3000 cycles showed that $Mg_{0.78}Cu_{0.22}O$ was still evenly distributed on the surface and did not fall off (Figure S12, Supporting Information). It was further illustrated that there was a strong interaction between $Mg_{0.78}Cu_{0.22}O$ and CuO/Cu_2O, which could effectively play a steric hindrance role to inhibit particle growth during long cycle. And $Mg_{0.78}Cu_{0.22}O$ could always provide oxygen vacancies on the surface to promote the redox

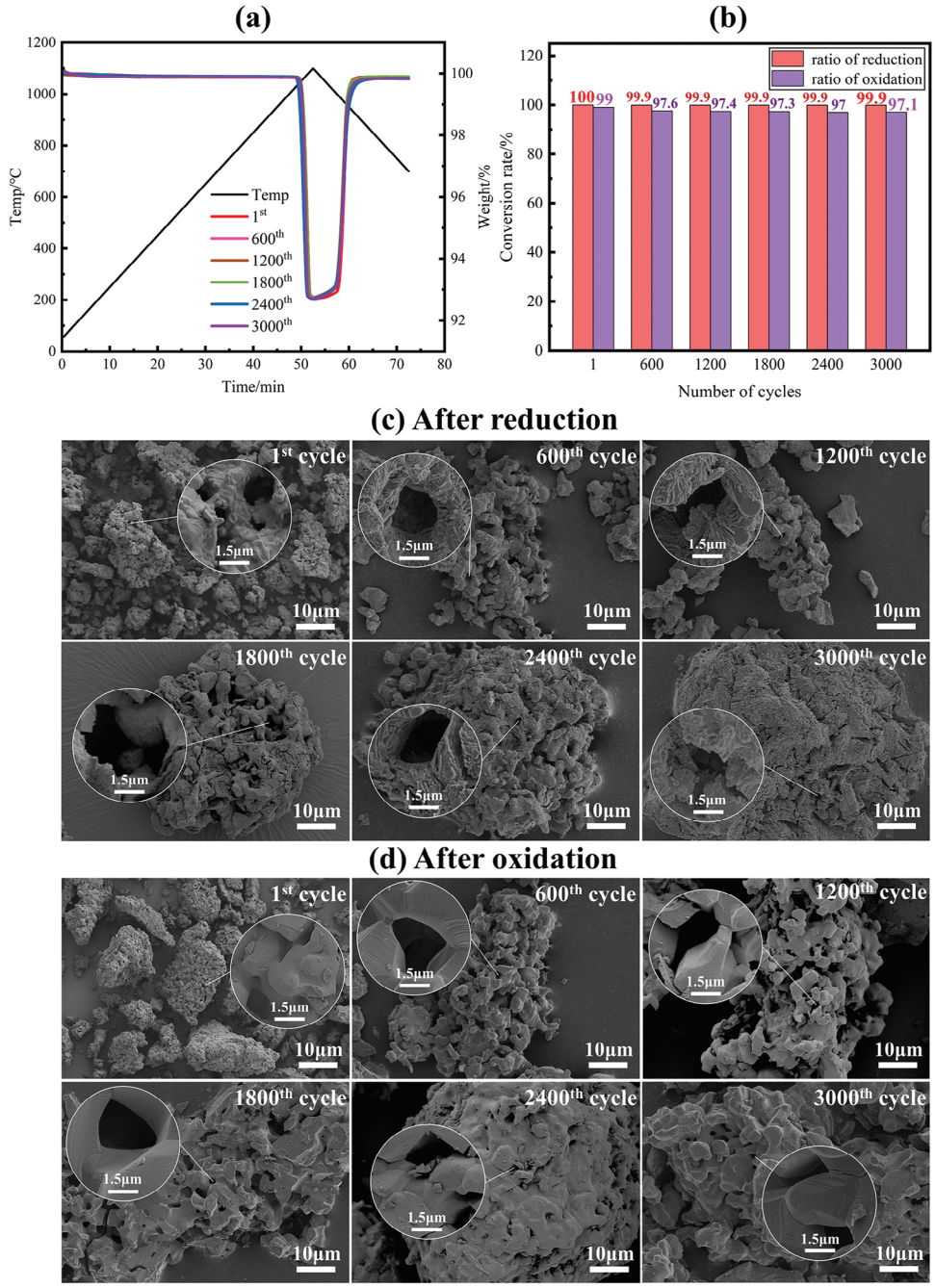

Figure 5. Cyclic stability testing and characterization of Cu-Mg-O. a) TG curves. b) conversion rate. FESEM images with different cycles: c) after reduction, (d) after oxidation.

reaction of Cu_2MgO_3/CuO/Cu_2O. Therefore, Cu-Mg-O had excellent long-term cycle stability.

2.6. Performance Improvement Mechanism

DFT calculation was used to further reveal the mechanism of Cu-Mg-O with reaction performance improvement. The results are shown in **Figure 6**. Material sintering greatly affects its reaction properties. According to the mass transfer through diffusion mechanism in solid state sintering theory, the vacancy concentration of each part of the particle has a certain difference. The concentration gradient promotes the diffusion and migration of thermal defects such as vacancies on the surface or inside of the particles, thus accelerating sintering.[36] Therefore, the formation energy of copper vacancies at different sites were calculated to explain the higher sintering temperature of Cu_2MgO_3 than CuO. Figure 6a shows that the E(V_{Cu}) of the two layers on the surface

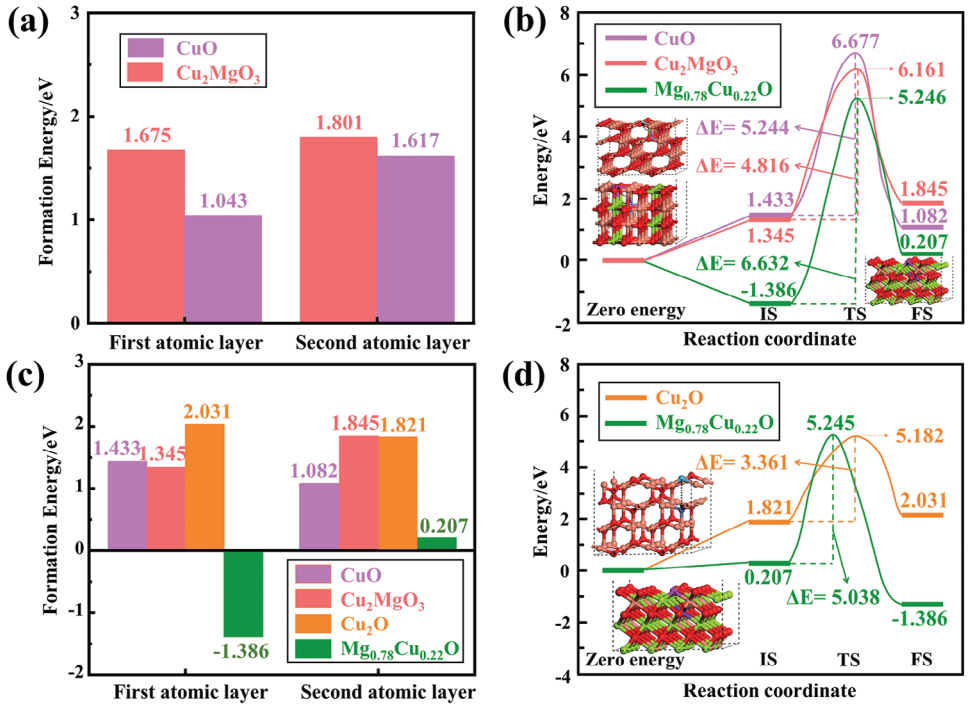

Figure 6. DFT calculation results. a) Formation energy of copper vacancies E(V_{Cu}) at different atomic layers of CuO and Cu_2MgO_3. b) Outward oxygen diffusion energy barriers ΔE during reduction. c) Formation energy of oxygen vacancies E(V_O) at different atomic layers of CuO, Cu_2MgO_3, Cu_2O and $Mg_{0.78}Cu_{0.22}O$. d) Inward oxygen diffusion energy barriers ΔE during oxidation.

of Cu_2MgO_3 (1.675 and 1.801 eV) are larger than those of CuO (1.043 and 1.617 eV). It demonstrates that Cu_2MgO_3 is more difficult to form copper vacancies for sintering than CuO, which clarifies the results of Figure 2 and Figure S4 (Supporting Information). In addition, the oxygen diffusion energy barrier ΔE was further compared to reveal the mechanism of excellent reduction reaction. The outward oxygen ion diffusion pathways of CuO and Cu_2MgO_3 are shown in Figures S13 and S14 (Supporting Information), respectively. As shown in Figure 6b, the ΔE of Cu_2MgO_3 is 4.816 eV smaller than that of CuO (5.244 eV). It elucidated that O^{2-} in Cu_2MgO_3 was easier to migrate for the reduction, shortening the reaction time (Figure 3d). Figures S15 and S16 (Supporting Information) show the formation energy of oxygen vacancies at different sites on the surface of Cu_2O and $Mg_{0.78}Cu_{0.22}O$ to determine the stable structure. As shown in Figure 6c, the formation energy of oxygen vacancies at the first and second atomic layers of $Mg_{0.78}Cu_{0.22}O$ are −1.386 and 0.207 eV, which are smaller than those of CuO (1.433 and 1.082 eV), Cu_2MgO_3 (1.345 and 1.845 eV) and Cu_2O (2.031 and 1.821 eV). It indicated that the surface of $Mg_{0.78}Cu_{0.22}O$ was easy to form oxygen vacancies, which was consistent with the results of XPS spectra of O 1s and low-temperature EPR (Figure 4d and Figure S8, Supporting Information). The outward migration path of oxygen ion of $Mg_{0.78}Cu_{0.22}O$ is shown in Figure S17 (Supporting Information). It can be seen from Figure 6b that its outward oxygen diffusion energy barrier ΔE (6.632 eV) is greater than that of CuO (5.244 eV) and Cu_2MgO_3 (4.816 eV). Figures S18 and S19 (Supporting Information) demonstrate the inward oxygen ion migration pathways of Cu_2O and $Mg_{0.78}Cu_{0.22}O$. Figure 6d also shows that the inward oxygen migration energy barrier of $Mg_{0.78}Cu_{0.22}O$ (5.038 eV) is larger than that of Cu_2O (3.361 eV). Based on these results, it was speculated that $Mg_{0.78}Cu_{0.22}O$ was easy to form oxygen vacancy, but it was a poor conductor of oxygen. Its surface was more likely to promote oxygen adsorption/desorption, but it didn't easily transport oxygen ions through the interior of the crystal during redox processes. $Mg_{0.78}Cu_{0.22}O$ might be facilitating easier and faster redox reactions of Cu_2MgO_3/CuO/Cu_2O by surface-assisted transfer of O.

It was worth mentioning that the experimental characterization results showed that $Mg_{0.78}Cu_{0.22}O$ also had a certain interaction with CuO and Cu_2O during the redox. Therefore, corresponding interface models were constructed for calculations to reveal the multiple effects of $Mg_{0.78}Cu_{0.22}O$. **Figure 7** shows the DFT calculation results. As shown in Figure 7a,b, the absolute values of the interfacial binding energies $|\Delta E_b|$ of CuO-$Mg_{0.78}Cu_{0.22}O$ (−18.060 eV) and Cu_2O-$Mg_{0.78}Cu_{0.22}O$ (−32.591 eV) are larger than CuO-CuO (−13.277 eV) and Cu_2O-Cu_2O (−12.299 eV). Figure 7c,d show the 3D charge density difference and planar averaged charge density difference along the Z direction of the corresponding interface model. The blue area and negative values indicated charge depletion, and the yellow area and positive values represented charge accumulation. The 3D charge density difference plot revealed that CuO-$Mg_{0.78}Cu_{0.22}O$ and Cu_2O-$Mg_{0.78}Cu_{0.22}O$ had more charge transfer at the interface compared to CuO-CuO and Cu_2O-Cu_2O. The planar averaged charge density difference along the Z direction gave a quantitative characterization of the charge distribution. As shown in Figure 7c, the maximum electron depletion and accumulation values at the CuO-$Mg_{0.78}Cu_{0.22}O$ interface are −2.843 and 2.335 e $Å^{-1}$, respectively. The maximum values

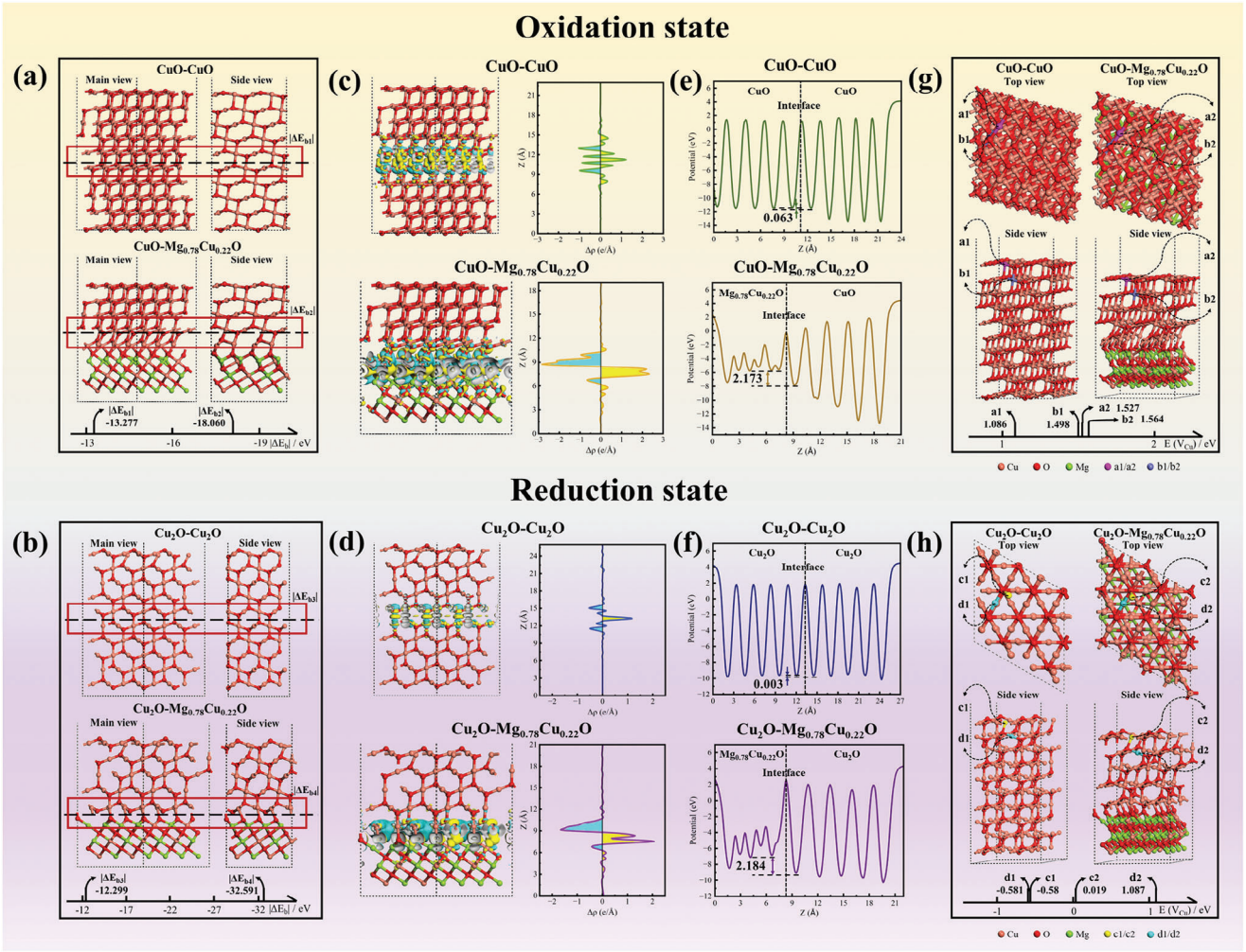

Figure 7. DFT calculation results. The absolute value of interface binding energy $|\Delta E_b|$: a) CuO-CuO and CuO-$Mg_{0.78}Cu_{0.22}O$, b) Cu_2O-Cu_2O and Cu_2O-$Mg_{0.78}Cu_{0.22}O$. The 3D charge density difference and planar averaged charge density difference along the Z direction: c) CuO-CuO and CuO-$Mg_{0.78}Cu_{0.22}O$, d) Cu_2O-Cu_2O and Cu_2O-$Mg_{0.78}Cu_{0.22}O$. The blue and yellow areas indicate electron depletion and accumulation, respectively. The isosurface value is set to be 0.0015 e $Å^{-1}$. The planar average electrotactic potential along the Z direction: e) CuO-CuO and CuO-$Mg_{0.78}Cu_{0.22}O$, f) Cu_2O-Cu_2O and Cu_2O-$Mg_{0.78}Cu_{0.22}O$. Formation energy of copper vacancies $E(V_{Cu})$ in interface structures: g) CuO-CuO and CuO-$Mg_{0.78}Cu_{0.22}O$, h) Cu_2O-Cu_2O and Cu_2O-$Mg_{0.78}Cu_{0.22}O$.

of CuO-CuO were −1.037 and 1.222 e $Å^{-1}$, which were significantly smaller than CuO-$Mg_{0.78}Cu_{0.22}O$. Figure 7d also shows that the maximum electron depletion and accumulation values at the Cu_2O-$Mg_{0.78}Cu_{0.22}O$ interface (−1.661 and 2.063 e $Å^{-1}$) are greater than those at Cu_2O-Cu_2O (−0.536 and 1.172 e $Å^{-1}$). This result again showed that CuO-$Mg_{0.78}Cu_{0.22}O$ and Cu_2O-$Mg_{0.78}Cu_{0.22}O$ had stronger charge transfer ability than CuO-CuO and Cu_2O-Cu_2O. Figure 7e,f present the planar average electrotactic potential along the Z direction curves. The calculation results in Figure 7e show that the potential difference of CuO-$Mg_{0.78}Cu_{0.22}O$ at the interface (2.173 eV) is much greater than that of CuO-CuO (0.063 eV). Figure 7f shows that the value at the Cu_2O-$Mg_{0.78}Cu_{0.22}O$ interface is 2.184 eV, while Cu_2O-Cu_2O is only 0.003 eV. The large average electrostatic potential difference facilitates the charge transfer at interface, which is consistent with the results of Figure 7c,d. In general, by calculating the interface characteristics, CuO/Cu_2O-$Mg_{0.78}Cu_{0.22}O$ had higher interfacial binding energy and stronger charge transfer ability due to strong interface interaction. This indicates that CuO/Cu_2O tend to bind to $Mg_{0.78}Cu_{0.22}O$ compared to CuO-CuO and Cu_2O-Cu_2O self-binding, which is consistent with the results of Figure 4b. This made the whole system more stable and effectively alleviated the coalescence and sintering caused by the surface contact and bonding of CuO/Cu_2O particles (Figure 2 and Figure S4, Supporting Information). The results of Table S4 (Supporting Information) show that the Cu—O and Mg—O bond lengths at the interface are shortened, which will increase the bond energy. Therefore, $Mg_{0.78}Cu_{0.22}O$ could still be firmly embedded on the surface of CuO/Cu_2O after long cycles (Figure 5c,d and Figure S12, Supporting Information). It was proved again that there was a strong interaction between $Mg_{0.78}Cu_{0.22}O$ and CuO/Cu_2O (Figure 4c). In order to further analyze the mechanism of sinter resistance improvement, the copper vacancy formation energy $E(V_{Cu})$ at different positions of the interface model was calculated. As

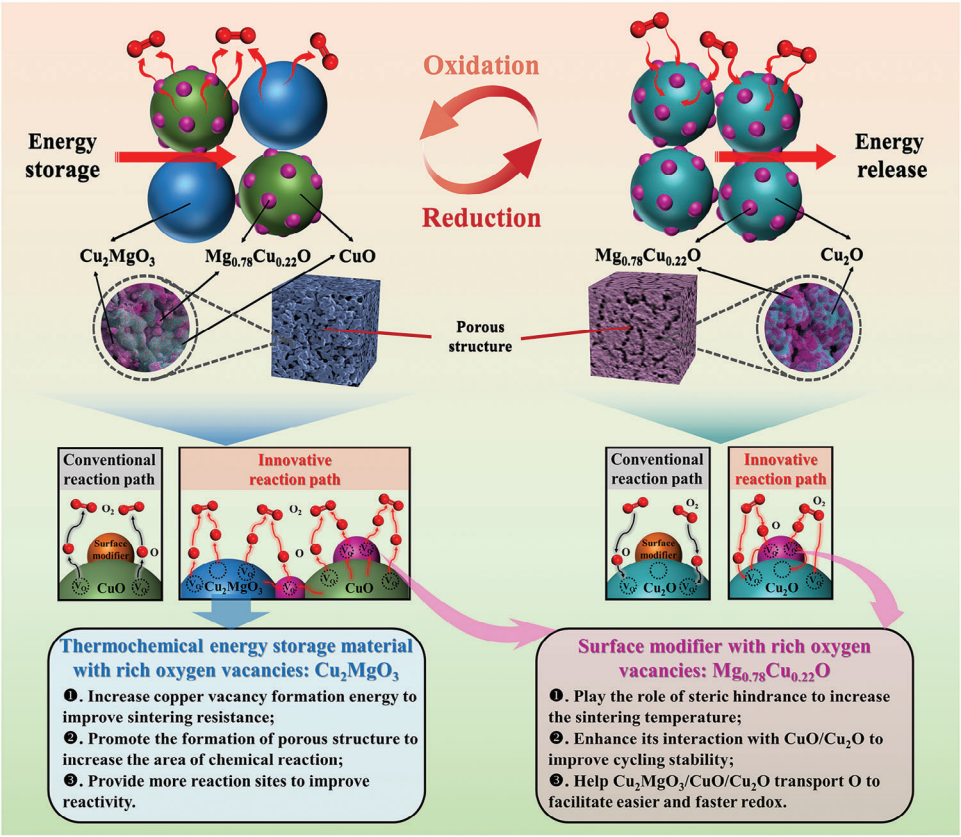

Figure 8. Schematic diagram of the Cu-Mg-O redox reaction mechanism and the innovation of this study.

shown in Figure 7g, the $E(V_{Cu})$ of different layers on the CuO-$Mg_{0.78}Cu_{0.22}O$ surface (1.527 and 1.564 eV) are greater than those of CuO-CuO (1.086 and 1.498 eV). The $E(V_{Cu})$ of reduced Cu_2O-$Mg_{0.78}Cu_{0.22}O$ (0.019 and 1.087 eV) in Figure 7h are also greater than Cu_2O-Cu_2O (−0.58 and −0.581 eV), respectively. It was shown that combining $Mg_{0.78}Cu_{0.22}O$ and CuO/Cu_2O could effectively avoid sintering caused by the mass transfer through copper vacancy diffusion. These calculations exhibited $Mg_{0.78}Cu_{0.22}O$ could effectively play the role of steric hindrance and improve the sintering temperature of the composite by enhancing the interaction and increasing the formation energy of copper vacancies of CuO/Cu_2O.

Combined with the results of experimental characterization and DFT calculations, the reaction mechanism of Cu-Mg-O in the redox process and the innovative reaction pathways are revealed (**Figure 8**). The composition of Cu-Mg-O after oxidation is Cu_2MgO_3, $Mg_{0.78}Cu_{0.22}O$ and CuO. Cu_2MgO_3 has a large number of oxygen vacancies that tend to aggregate and merge, thus promoting the formation of porous structure. The structure is conducive to the uniform distribution of heat and gas. And Cu_2MgO_3 has higher copper vacancy formation energy, which can effectively improve the sintering resistance of composite. Meanwhile, oxygen vacancies provide more reaction sites to facilitate the reduction reaction of Cu_2MgO_3. And its oxygen migration energy barrier is lower than CuO, which is more prone to reduction reaction. The composition of Cu-Mg-O after reduction is $Mg_{0.78}Cu_{0.22}O$ and Cu_2O. Compared with the traditional artificial addition of chemically stable surface modifiers to alleviate the sintering of CuO/Cu_2O. Cu-Mg-O spontaneously generates $Mg_{0.78}Cu_{0.22}O$ during the first reaction, and continue to be evenly distributed on the CuO/Cu_2O grain boundary in the subsequent cycles. The driving force of CuO/Cu_2O grain growth is offset by the Zener pinning force of $Mg_{0.78}Cu_{0.22}O$ acting at the grain boundary, which can effectively inhibit the grain growth.[37] It also effectively exerts the steric hindrance effect and increases the copper vacancy formation energy of CuO/Cu_2O, which restricts the coalescence of particles and diffusion mass transfer to increase the sintering temperature. The strong interaction between $Mg_{0.78}Cu_{0.22}O$ and CuO/Cu_2O ensures that $Mg_{0.78}Cu_{0.22}O$ does not fall off during multiple cycles, which greatly enhances the cycling stability. In addition, the oxygen vacancy-rich $Mg_{0.78}Cu_{0.22}O$ further helps Cu_2MgO_3/CuO/Cu_2O transfer O through the surface rather than inside the crystals to promote easier and faster redox reactions in this system. Moreover, the porous structure of the composite has been maintained throughout the reversible reaction process and long cycles, which can increase the chemical reaction contact area to improve the reaction kinetics. Therefore, Cu-Mg-O has excellent high temperature sintering resistance and long-cycle reactivity.

3. Conclusion

In summary, we have successfully constructed oxygen vacancy-rich defects porous Cu_2MgO_3/$Mg_{0.78}Cu_{0.22}O$ composite

structure. The composite was labeled Cu-Mg-O. And Cu-Mg-O was synthesized by a simple high-temperature heat treatment method. It only had slight sintering in the high temperature working range, showing excellent sintering resistance. Cu-Mg-O was up to 99% compared to the 46% re-oxidation degree of CuO. Its energy storage and release densities were −362.822 and 357.009 kJ kg^{-1} with outstanding chemical reversibility. The energy release reaction rate was increased by 3.5 times. The number of cycles of the reported modified Cu-based materials is basically less than 100 cycles. Surprisingly, Cu-Mg-O still retained 99.9% and 97.1% reduction and oxidation reactivity after 3000 cycles. The porous structure was well showed, and $Mg_{0.78}Cu_{0.22}O$ was uniformly dispersed on the CuO/Cu_2O surface. Combined with experimental characterization and DFT calculations, we confirmed the effectiveness of the innovative method proposed in this study. And we revealed the mechanism of the performance improvement and new findings of Cu-Mg-O. The composition of Cu-Mg-O after oxidation was Cu_2MgO_3, $Mg_{0.78}Cu_{0.22}O$ and CuO. Cu_2MgO_3 had a large $E(V_{Cu})$ that was more difficult to sinter. And its oxygen diffusion energy barrier ΔE was lower than that of CuO and easier to reduce. Moreover, Cu_2MgO_3 and $Mg_{0.78}Cu_{0.22}O$ had low $E(V_O)$. Therefore, there were a large number of oxygen vacancies in the materials to promote the formation of a porous structure, which helped to evenly distribute heat and provide more reactive sites. Thus its reduction activity could remain 99.9% after 3000 cycles. The composition of Cu-Mg-O after reduction was $Mg_{0.78}Cu_{0.22}O$ and Cu_2O. $Mg_{0.78}Cu_{0.22}O$ existed in the whole redox process, but its oxygen migration energy barrier ΔE was high. It was speculated that it helped $Cu_2MgO_3/CuO/Cu_2O$ transfer more O faster from the surface to facilitate the reaction. In addition, $Mg_{0.78}Cu_{0.22}O$ had a larger binding energy with CuO/Cu_2O than CuO/Cu_2O self-binding. And there was more charge transfer and bond energy enhancement at the interface junction. The presence of a strong interaction between them was confirmed. It ensured that $Mg_{0.78}Cu_{0.22}O$ could still be firmly dispersed on the surface of Cu_2O/CuO after long cycles. And the copper vacancy formation energy of CuO/Cu_2O was increased after the combination. It effectively solved the sintering problems caused by contact of CuO/Cu_2O particles and mass transfer. Therefore, Cu-Mg-O had excellent cyclic reactivity. This work can provide insights into the development of high-performance thermochemical energy storage materials.

4. Experimental Section

Material Preparation: Cu_2MgO_3 was prepared by the simple high-temperature solid-phase method. CuO and MgO with a molar ratio of 1.5:1, 2:1, and 2.5:1 were weighed, respectively. These powders were uniformly mixed in a planetary ball mill for 30 min. Finally, the composite could be obtained by calcining at 1000 °C for 5 h. In this paper, Cu-Mg-O represent the prepared sample with a molar ratio of 2:1.

Material Testing and Characterizations: The simultaneous thermal analysis (TGA/DSC3+) was used for measuring the energy storage/release performance. The test conditions were air atmosphere with a flow rate of 50 mL $mi^{-1}n$, heating from 50 °C to 1100 °C and then cooling from 1100 °C to 700 °C at a heating/cooling rate of 20 °C min^{-1}. Reduction reaction (endothermic) occurred during heating, followed by oxidation (exothermic) occurred during cooling. The crystal structure and phase composition of the samples at different stages were recorded by powder X-ray diffraction (XRD) in the range of 2θ of 10–80°. It was performed on an X'Pert Powder diffractometer equipped with Cu Kα radiation source (λ = 1.5406 Å) operating at 40 kV and 40 mA. The scanning rate was 0.02° and 20 s counting time per angle. The chemical bonds in the various samples were further identified by Fourier transform infrared (FTIR) spectra on a Thermo Scientific Nicolet iS20 spectrometer using KBr pellets in the range of 4000–400 cm^{-1} with a resolution of 4 cm^{-1}. The X-ray photoelectron spectroscopy (XPS) was used to analyze the surface chemistry of composite. It was performed on a Thermo Scientific K-Alpha electron energy analyzer with monochromatic Al Kα (1486.6 eV) radiation, which was operated at 15 kV. Low-temperature electron paramagnetic resonance (EPR) tests were performed on a Bruker ESRA-300 spectrometer. The micromorphology and element distribution of the samples were investigated by field emission scanning electron microscopy-energy-dispersive spectroscopy (FESEM-EDS) on a SU-8010 microscope equipped with an Oxford X-max80 spectrometer.

DFT Computation: Calculations were performed using density functional theory (DFT) as implemented in the Vienna ab initio simulation package (VASP).[38] The generalized gradient approximation (GGA) with the Perdew-Burke-Ernzerhof (PBE) exchange-correlation function was applied.[39] The projector-augmented wave (PAW) method was used to describe the core-valence interaction.[40] The strong 3d electron correlation effect of Cu was accurately addressed using the DFT + U method.[41] The U = 7 eV was set for the Cu.[42] The planewave basis set was obtained with a kinetic energy cutoff of 500 eV. The convergence criterion for the total energy was employed to 1.0×10^{-4} eV, and for all of the atoms until the residual force was less than 0.02 eV $Å^{-1}$. Table S1 (Supporting Information) shows the Monkhorst-Pack k-point grid settings. It was worth mentioning that $Mg_{0.78}Cu_{0.22}O$ in this paper was actually $Mg_{0.75}Cu_{0.25}O$ by artificially replacing one of the four Mg atoms in the MgO unit cell with a Cu atom. In order to reduce the volume of the model during calculation, an approximate treatment was adopted to equivalent it to $Mg_{0.78}Cu_{0.22}O$. As shown in Table S2 (Supporting Information), the lattice parameters optimized by DFT were in good agreement with the experiments with small deviations. This showed that the DFT calculation was reliable for geometric optimization. Previous studies have shown that CuO (111), Cu_2O (111), and MgO (111) were stable low-index surfaces and were more easily exposed to the environment.[43,44] In addition, the surface energy of different terminals of Cu_2MgO_3, was calculated and the results were shown in Figure S1 (Supporting Information). Compared with other surfaces, (100) had the lowest surface energy (0.796 J m^{-2}), indicating that it was the most stable surface. Consequently, CuO (111), Cu_2O (111), $Mg_{0.78}Cu_{0.22}O$ (111) and Cu_2MgO_3 (100) surface was used to investigate the redox reaction mechanism. For the slab calculations, a slab/vacuum geometry was adopted and further expanded by the supercell method into a $p(2 \times 2)$ surface unit cell. To avoid the interactions between slabs, a vacuum thickness of 20 Å was generated for all slab models. The detailed structural parameters of slab models were listed in Table S3 (Supporting Information). For the oxygen diffusion barrier calculation, the transition state was optimized by relaxing the force below 0.02 eV $Å^{-1}$ using the climbing image nudged elastic band (CI-NEB) method.[45]

Supporting Information

Supporting Information is available from the Wiley Online Library or from the author.

Acknowledgements

This work was supported by the National Natural Science Foundation of China (52325605) and the Fundamental Research Funds for the Central Universities (2022ZFJH04).

Conflict of Interest

The authors declare no conflict of interest.

Data Availability Statement

The data that support the findings of this study are available from the corresponding author upon reasonable request.

Keywords

long cycle reactivity, modification mechanism, oxygen vacancy-rich defects, sinter-resistant, thermochemical energy storage

Received: December 6, 2023
Revised: January 3, 2024
Published online: March 21, 2024

[1] X. Peng, M. Yao, T. W. Root, C. T. Maravelias, *Appl. Energy* **2020**, *262*, 114543.
[2] Y. L. He, Y. Qiu, K. Wang, F. Yuan, W. Q. Wang, M. J. Li, J. Q. Guo, *Energy* **2020**, *198*, 117373.
[3] L. A. Weinstein, J. Loomis, B. Bhatia, D. M. Bierman, E. N. Wang, G. Chen, *Chem. Rev.* **2015**, *115*, 12797.
[4] A. J. Carrillo, J. González-Aguilar, M. Romero, J. M. Coronado, *Chem. Rev.* **2019**, *119*, 4777.
[5] S. Wu, C. Zhou, E. Doroodchi, R. Nellore, B. Moghtaderi, *Energy Convers. Manage.* **2018**, *168*, 421.
[6] X. Y. Han, L. Wang, H. S. Ling, Z. W. Ge, X. P. Lin, X. J. Dai, H. S. Chen, *Renew. Sustain. Energy Rev.* **2022**, *158*, 112076.
[7] A. S. Padilla, H. R. P. Rubio, *J. Energy Storage* **2023**, *73*, 108906.
[8] C. Agrafiotis, M. Roeb, M. Schmücker, C. Sattler, *Sol. Energy* **2014**, *102*, 189.
[9] C. Agrafiotis, S. Tescari, M. Roeb, M. Schmücker, C. Sattler, *Sol. Energy* **2015**, *114*, 459.
[10] A. J. Schrader, A. P. Muroyama, P. G. Loutzenhiser, *Sol. Energy* **2015**, *118*, 485.
[11] D. Müller, C. Knoll, W. Artner, M. Harasek, C. Gierl-Mayer, J. M. Welch, A. Werner, P. Weinberger, *Sol. Energy* **2017**, *153*, 11.
[12] N. Nekokar, M. Pourabdoli, A. G. Hamidi, D. Uner, *Adv. Powder Technol.* **2018**, *29*, 333.
[13] D. Xiang, C. Gu, H. Xu, G. Xiao, *Small* **2021**, *17*, 2101524.
[14] D. Yilmaz, E. Darwish, H. Leion, *J. Energy Storage* **2020**, *28*, 101180.
[15] J. Liu, J. Baeyens, Y. Deng, X. Wang, H. Zhang, *J. Environ. Manage.* **2020**, *267*, 110582.
[16] A. J. Carrillo, P. Pizarro, J. M. Coronado, *J. Energy Storage* **2021**, *33*, 102028.
[17] J. Moya, J. Marugán, M. Orfila, M. A. Diaz-Perez, J. C. Serrano-Ruiz, *Molecules* **2021**, *26*, 583.
[18] M. Neises, S. Tescari, L. de Oliveira, M. Roeb, C. Sattler, B. Wong, *Sol. Energy* **2012**, *86*, 3040.
[19] R. D. Schmidt-Whitley, M. Martinez-Clemente, A. Revcolevschi, *J. Cryst. Growth* **1974**, *23*, 113.
[20] M. Deutsch, F. Horvath, C. Knoll, D. Lager, C. Gierl-Mayer, P. Weinberger, F. Winter, *Energy Fuels* **2017**, *31*, 2324.
[21] E. Alonso, C. Pérez-Rábago, J. Licurgo, E. Fuentealba, C. A. Estrada, *Sol. Energy* **2015**, *115*, 297.
[22] M. Deutsch, F. Horvath, C. Knoll, D. Lager, C. Gierl-Mayer, P. Weinberger, F. Winter, *Energy Fuels* **2017**, *31*, 2324.
[23] M. Gigantino, S. Sas Brunser, A. Steinfeld, *Energy Fuels* **2020**, *34*, 16772.
[24] D. Xiang, C. Gu, H. Xu, J. Deng, P. Zhu, G. Xiao, *ACS Appl. Mater. Interfaces.* **2021**, *13*, 57274.
[25] J. L. Deng, C. D. Gu, H. R. Xu, G. Xiao, *ACS Appl. Mater. Interfaces.* **2022**, *14*, 43151.
[26] J. L. Deng, C. D. Gu, H. R. Xu, G. Xiao, *J. Energy Storage* **2023**, *59*, 106370.
[27] M. Sun, Y. Lei, H. Cheng, J. Ma, Y. Qin, Y. Kong, S. Komarneni, *J. Alloys Compd.* **2020**, *825*, 154036.
[28] S. Guo, M. Liu, L. You, G. Cheng, J. Li, K. Zhou, *Chemosphere* **2021**, *279*, 130482.
[29] G. Karunakaran, M. Kundu, S. Kumari, E. Kolesnikov, M. V. Gorshenkov, G. Maduraiveeran, M. Sasidharan, D. Kuznetsov, *J. Alloys Compd.* **2018**, *763*, 94.
[30] M. Mandal, R. Nagaraj, K. Chattopadhyay, M. Chakraborty, S. Chatterjee, D. Ghosh, S. K. Bhattacharya, *J. Mater. Sci.* **2021**, *56*, 3325.
[31] H. Hamad, M. M. Elsenety, W. Sadik, A. G. El-Demerdash, A. Nashed, A. Mostafa, S. Elyamny, *Sci. Rep.* **2022**, *12*, 2217.
[32] K. Qian, R. You, Y. Guan, W. Wen, Y. C. Tian, Y. Pan, W. X. Huang, *ACS Catal.* **2020**, *10*, 15142.
[33] S. Abuelgasim, T. L. Li, Y. G. Cao, W. J. Wang, A. Abdalazeez, C. L. Liu, *Sep. Purif. Technol.* **2022**, *302*, 122136.
[34] N. Zayyoun, L. Bahmad, L. Laânab, B. Jaber, *Appl. Phys. A* **2016**, *122*, 488.
[35] M. Elango, M. Deepa, R. Subramanian, A. M. Musthafa, *Polym.-Plast. Technol. Eng.* **2018**, *57*, 1440.
[36] H. Djohari, J. I. Martínez-Herrera, J. J. Derby, *Chem. Eng. Sci.* **2009**, *64*, 3799.
[37] C. S. Smith, *Trans. Metall. Soc. AIME* **1948**, *175*, 15.
[38] G. Kresse, J. Furthmüller, *Phys. Rev. B* **1996**, *54*, 11169.
[39] J. P. Perdew, K. Burke, M. Ernzerhof, *Phys. Rev. Lett.* **1996**, *77*, 3865.
[40] G. Kresse, D. Joubert, *Phys. Rev. B* **1999**, *59*, 1758.
[41] S. L. Dudarev, G. A. Botton, S. Y. Savrasov, C. J. Humphreys, A. P. Sutton, *Phys. Rev. B* **1998**, *57*, 1505.
[42] M. Nolan, S. D. Elliott, *Phys. Chem. Chem. Phys.* **2006**, *8*, 5350.
[43] F. Chiter, D. Costa, V. Maurice, P. Marcus, *J. Phys. Chem. C* **2020**, *124*, 17048.
[44] H. H. Fang, S. Wu, T. Ayvali, J. W. Zheng, J. Fellowes, P.-L. Ho, K. C. Leung, A. Large, G. Held, R. Kato, K. Suenaga, Y. I. A. Reyes, H. V. Thang, H.-Y. T. Chen, S. C. E. Tsang, *Nat. Commun.* **2023**, *14*, 647.
[45] G. Henkelman, B. P. Uberuaga, H. Jónsson, *J. Chem. Phys.* **2000**, *113*, 9901.

